Environmental Science Nano

ROYAL SOCIETY OF CHEMISTRY

PAPER

View Article Online
View Journal | View Issue

Cite this: *Environ. Sci.: Nano*, 2021, 8, 711

Carbon–titanium dioxide (C/TiO_2) nanofiber composites for chemical oxidation of emerging organic contaminants in reactive filtration applications†

Katherine E. Greenstein,[a] Matthew R. Nagorzanski,[a] Bailey Kelsay,[a] Edgard M. Verdugo,[a] Nosang V. Myung,[b] Gene F. Parkin[a] and David M. Cwiertny *[ac]

The recalcitrance of some emerging organic contaminants through conventional water treatment systems may necessitate advanced technologies that use highly reactive, non-specific hydroxyl radicals. Here, polyacrylonitrile (PAN) nanofibers with embedded titanium dioxide (TiO_2) nanoparticles were synthesized *via* electrospinning and subsequently carbonized to produce mechanically stable carbon/TiO_2 (C/TiO_2) nanofiber composite filters. Nanofiber composites were optimized for reactivity in flow through treatment systems by varying their mass loading of TiO_2, adding phthalic acid (PTA) as a dispersing agent for nanoparticles in electrospinning sol gels, comparing different types of commercially available TiO_2 nanoparticles (Aeroxide® P25 and 5 nm anatase nanoparticles) and through functionalization with gold (Au/TiO_2) as a co-catalyst. High bulk and surface TiO_2 concentrations correspond with enhanced nanofiber reactivity, while PTA as a dispersant makes it possible to fabricate materials at very high P25 loadings (~80% wt%). The optimal composite formulation (50 wt% P25 with 2.5 wt% PTA) combining high reactivity and material stability was then tested across a range of variables relevant to filtration applications including filter thickness (300–1800 μm), permeate flux (from 540–2700 L m^{-2} h), incident light energy (UV-254 and simulated sunlight), flow configuration (dead-end and cross-flow filtration), presence of potentially interfering co-solutes (dissolved organic matter and carbonate alkalinity), and across a suite of eight organic micropollutants (atrazine, benzotriazole, caffeine, carbamazepine, DEET, metoprolol, naproxen, and sulfamethoxazole). During cross-flow recirculation under UV-irradiation, 300 μm thick filters (30 mg total mass) produced micropollutant half-lives ~45 min, with 40–90% removal (from an initial 0.5 μM concentration) in a single pass through the filter. The initial reaction rate coefficients of micropollutant transformation did not clearly correlate with reported second order rate coefficients for reaction with hydroxyl radical (k_{OH}), implying that processes other than reaction with photogenerated hydroxyl radical (*e.g.*, surface sorption) may control the overall rate of transformation. The materials developed herein represent a promising next-generation filtration technology that integrates photocatalytic activity in a robust platform for nanomaterial-enabled water treatment.

Received 22nd September 2020,
Accepted 3rd February 2021

DOI: 10.1039/d0en00975j

rsc.li/es-nano

Environmental significance

For water treatment applications, functionalized nanocomposites hold promise for integrating reactive nanoparticles into a stable and scalable platform. Here, we fabricate, optimize and demonstrate the performance of electrospun carbon nanofibers with integrated photocatalytic titanium dioxide for use as reactive filtration materials. We illustrate the viability of these materials for advanced oxidation processes in a flow through filtration system targeting a suite of otherwise recalcitrant constituents of emerging concern in complex matrices representative of source and finished drinking water. We envision that these carbon–titanium dioxide nanofiber filters are ideal for decentralized water treatment (*e.g.*, point of use and entry systems), where versatile, multi-functional technologies are needed to address complex water quality challenges in a small technology footprint.

[a] *Department of Civil and Environmental Engineering, University of Iowa, 4105 Seamans Center, Iowa City, IA 52242, USA. E-mail: david-cwiertny@uiowa.edu; Fax: +1 319 335 5660; Tel: +1 319 335 1401*
[b] *Department of Chemical and Biomolecular Engineering, University of Notre Dame, IN 46556, USA*
[c] *Department of Chemical and Biochemical Engineering, University of Iowa, Iowa City, IA 52242, USA*

† Electronic supplementary information (ESI) available. See DOI: 10.1039/d0en00975j

1. Introduction

To address more recalcitrant pollutant classes, the use of titanium dioxide (TiO_2) as a photocatalyst for advanced oxidation processes (AOPs) remains widely studied[1–3] despite well-recognized barriers to its practical implementation.[4–6] Because commercially available nanoparticle catalysts (*i.e.*, Aeroxide® P25) can be challenging to deploy as dispersions at water treatment scale, we recently explored the potential of using three-dimensional networks of TiO_2 nanofibers fabricated *via* electrospinning[7] as an alternative platform for coupling chemical oxidation processes for dissolved micropollutants with filtration (*i.e.*, removal of suspended particles *via* physical capture within the nanofiber network).[8] Unfortunately, we,[7] and others,[9] have found nanofibers of pure TiO_2 to be brittle and thus not practically viable as a stand-alone platform when compared with more robust polymeric[10] or even carbon nanofibers (CNFs)[11] generated *via* electrospinning.

To develop a cohesive electrospun platform that balances material strength and reactivity, recent studies have explored the immobilization of TiO_2 nanoparticles on or within polymeric electrospun nanofibers [*e.g.*, cellulose or polyacrylonitrile (PAN)].[12] Several synthesis approaches are common, including (i) direct addition of TiO_2 nanoparticles or nanorods into electrospinning precursor solutions;[13–15] (ii) incorporation of Ti-containing compounds (*e.g.*, titanium tetraisopropoxide) into electrospinning precursor solutions with post-processing to form *in situ* TiO_2 nanoparticles;[16–19] and (iii) hydrothermal treatment of previously fabricated nanofibers for TiO_2 surface deposition.[20–22] Many of these have been fabricated for applications beyond water treatment, including air purification[21,23,24] and oil–water separation.[25]

Of those most relevant to technology development for water treatment, the majority have focused on treatment targets (*e.g.*, dyes) of limited relevance to the current challenges of water treatment providers resulting from emerging pollutant classes.[15,22] In one noteworthy study, PVDF nanofibers electrosprayed with TiO_2 nanoparticles were used for oxidation of bisphenol A, 4-chlorophenol, and cimetidine.[26] However, the multiple synthesis steps required and concern over stability of surface deposited TiO_2 (as opposed to TiO_2 integrated into nanofibers) may still limit the viability of such composite materials for water treatment. In another report, PAN nanofibers containing a Ti precursor were treated hydrothermally to grow TiO_2 *in situ* and then demonstrated for oxidation of phenol, a model hydroxyl radical probe compound.[19] However, PAN, which contains electron rich nitrile groups, likely scavenged some of the hydroxyl radical species, reducing treatment efficiency.[19] In addition, although PVDF is expected to withstand the oxidants generated by TiO_2/UV, many polymers, including PAN, are not similarly resistant to oxidation.[27]

Carbon is likely a more promising material for a TiO_2 composite; it can withstand the oxidative environment created by TiO_2/UV, and it may also function as sorbent that can concentrate some organic targets for subsequent degradation by photogenerated hydroxyl radicals ($^{\bullet}OH$) likely to be most concentrated at the composite surface. Nevertheless, development and performance assessments of carbon/TiO_2 nanofiber composites remain sparse and have thus far primarily centered on hydrothermal growth or solvothermal synthesis of TiO_2 nanostructures on pre-fabricated electrospun CNFs.[28,29] These syntheses demand post-processing of electrospun and stabilized/carbonized nanofibers, which adds to the complexity and time required for making materials. Further, CNFs can also suffer from being as brittle and low in material strength as most, pure inorganic nanofibers, which leaves their viability as reactive water filtration platforms in question. Indeed, several reactivity studies with carbon/TiO_2 reactivity have been conducted in batch suspensions after breaking up (*i.e.*, dispersing) the carbon/TiO_2 nanofibers (as we previously did for pure TiO_2 nanofibers),[7] thereby neglecting any consideration of material strength during composite development.[28,29] It is worth noting, that as with polymer composites, most of this work with carbon-based composites has yet to demonstrate nanofiber performance in conditions representative of water treatment, often focusing on photocatalytic removal of dyes (*e.g.*, methylene blue, methyl orange, and acid red) at relatively high (5–15 mg L^{-1}) concentrations.[28,29]

Herein, we develop a TiO_2-based nanofiber composite *via* an electrospinning synthesis that (i) is simplified (*i.e.*, single-pot); (ii) improves material strength, durability and flexibility relative to pure TiO_2 nanofibers; and (iii) enables photocatalytic reactivity in a flow through platform able to target the most persistent organic micropollutants during conventional water treatment. We use a single-pot electrospinning method to produce polyacrylonitrile (PAN) nanofibers with embedded Aeroxide® P25 nanoparticles (a commercially available TiO_2 photocatalyst with bandgap of 3.2 eV, corresponding to an excitation wavelength of ~390 nm),[30] where subsequent stabilization/carbonization is used to convert PAN into a flexible and photochemically active carbon/titanium dioxide (C/TiO_2) composite. Using this approach, we demonstrate the ability to electrospin PAN/TiO_2 composites with up to 80 wt% TiO_2 relative to PAN with aid of an organic acid dispersant, phthalic acid, producing a nanofiber framework mostly comprised of TiO_2 but that still retains some strength and flexibility after carbonization.

For a suite of systematically tailored C/TiO_2 composites, we assessed and optimized the nanofiber properties most influential on material photocatalytic activity toward atrazine, a widely applied organic herbicide and regulated contaminant in drinking water. Composite variables explored included (i) mass loading of TiO_2; (ii) concentration of phthalic acid incorporated into electrospinning precursor solutions; and (iii) the type and size of TiO_2 nanoparticles [*e.g.*, mixed-phase Aeroxide® P25 with ~21 nm diameter, 5

nm anatase TiO_2 nanoparticles, and P25 with deposited gold as a co-catalyst (Au/TiO_2)]. All reactivity studies toward atrazine were conducted in a cross-flow UV microfiltration apparatus, and thus we also explored how process flow rate and the thickness of the photoactive composite nanofiber network (tailored by the volume of electrospinning precursor used in fabrication) influenced atrazine removal efficiencies. Ultimately, the performance of the optimal C/TiO_2 composite was tested toward a suite of organic micropollutants frequently detected in drinking water that are recalcitrant to conventional treatment[31–33] including benzotriazole, carbamazepine, DEET, metoprolol, and sulfamethoxazole, and in matrices representative of water treatment, revealing these composites to be a promising hybrid filtration-advanced oxidation process for water treatment.

2. Experimental methods

2.1. Reagents

A complete list of reagents can be found in the ESI.†

2.2. Synthesis of C/TiO_2 composites

PAN nanofibers containing phthalic acid (PTA) and seeded with TiO_2 nanoparticles were electrospun, stabilized, and carbonized to obtain C/TiO_2 composite nanofiber filters. Nanofibers were prepared to assess the impact of TiO_2 nanoparticle size, phase composition, and mass loading in CNFs, as well as the impact of PTA (both as a dispersant for TiO_2 in sol gels and to introduce nanofiber porosity)[11] on C/TiO_2 composite flexibility and reactivity. Either 5 nm TiO_2 (anatase) or Aeroxide® P25 (~75% : 25% anatase : rutile; ~21 nm in diameter) nanoparticles were suspended in DMF (from 1 to 7 mL) with either no PTA or 2.5 wt% PTA (relative to total sol gel mass) and sonicated for 5 h. PAN (8 wt% relative to DMF) was added and dissolved by thermally mixing the solution at 60 °C for 2 h. For assessment of P25 mass loading on reactivity, 15 to 80 wt% P25 was added to sol gels along with 2.5 wt% PTA. To evaluate the effect of PTA, sol gels with either 50 wt% P25 or 50 wt% 5 nm TiO_2 were prepared both free of PTA and with 2.5 wt% PTA. These sol gels were also used to compare the effect of TiO_2 nanoparticle size and phase on composite reactivity. Finally, because noble metals co-catalyst can improve TiO_2 photocatalytic performance,[7] a subset of composites were prepared using gold-functionalized P25 particles (*i.e.*, Au/TiO_2) that were prepared *via* the dropwise reduction of 1 mM Au(III) chloride with 10 mM ascorbic acid in a suspension of P25 nanoparticles (2 g L^{-1} with 150 mL total volume; full synthesis details are in the ESI†). Assuming complete deposition, this would produce an Au loading of 1.5 wt%. In our prior work,[7] we used a similar method with urea as the reductant to deposit ~2–5 nm Au nanoparticles on TiO_2.

After cooling to room temperature following thermal mixing, prepared sol gels were electrospun with a 23G needle and 15 kV/10 cm with a flow rate of 0.5 mL h^{-1} using a previously described system.[11] The electrospinning process was ceased after 6 h, and the mat was peeled off the Al foil-coated grounded collector. Electrospun PAN/TiO_2 nanofibers were then stabilized at 250 °C in air for 2.5 h and carbonized at 450 °C in nitrogen (N_2) for 1 h in a tube furnace (MTI OTF 1200x) (with ramp rate of 5 °C min^{-1}). This relatively low annealing temperature was used to produce an amorphous carbon likely to exhibit mechanical properties (*e.g.*, flexibility, not brittle) necessary for use in water filtration applications. After stabilization and carbonization, nanofiber mats were cut into circles with diameter of 47 mm for use in reactive filtration experiments.

2.3. Nanofiber filter characterization

C/TiO_2 nanofiber composites were characterized to ascertain their chemical and physical properties. Filter thickness and nanofiber diameter were quantified with a Hitachi S-4800 scanning electron microscope (SEM) as in our prior work.[7] Briefly, filter thickness was determined by cross-sectional imaging of C/TiO_2 mats, whereas the average nanofiber diameter within a filter was determined from measurement of at least 100 nanofibers. In both cases, dimensions in SEM images were sized using the software program ImageJ. SEM imaging was also used to evaluate the TiO_2 abundance and distribution in all C/TiO_2 materials, as well as the presence or absence of pores introduced by PTA. The phase of TiO_2 nanoparticles embedded in composites was confirmed with X-ray diffraction (XRD, Rigaku MiniFlexII, Co X-ray source). N_2-BET analysis (Quantachrome Nova 4200e) was used to determine surface area of nanofiber composites after outgassing samples at 60 °C for 6 h prior to measurement. Due to the amount of material consumed during N_2-BET measurements, we only conducted single analyses on select, high priority samples. Relative abundance of Ti on the surface of nanofibers was analyzed with a Kratos Axis Ultra X-ray photoelectron spectroscopy (XPS) system equipped with a monochromatic Al Kα X-ray source. Additional details related to sample preparation for material characterization are provided in the ESI.†

2.4. Photocatalytic filtration experiments

Composite nanofiber filter performance was assessed in a custom-built cross-flow filtration apparatus with integrated quartz window to allow UV or simulated sunlight irradiation during operation. A 47 mm diameter nanofiber filter was supported with a 0.22 μm PVDF filter (Durapore) and placed into a Millipore filter holder modified with a 38 mm diameter quartz window (see schematic in Fig. S1†). During photocatalytic filtration experiments, the quartz window was exposed to UV light from an Hg(Xe) arc lamp (Newport, 200 W) with a 250 nm cut-on long-pass filter (Asahi Spectra) or a 305 nm cut-on long-pass filter (for a limited number of experiments simulating sunlight). The spectral irradiance of this source is shown in Fig. S2.†

The majority of experiments was conducted with 500 mL of test solution prepared using 5 mM phosphate buffer

adjusted to pH 7 spiked with 0.14 (30 μg L^{-1} or 10-times the US EPA maximum contaminant limit or MCL), 0.5 or 2 μM of atrazine. Experiments were also conducted with 0.5 μM of benzotriazole, caffeine, carbamazepine, DEET, metoprolol, naproxen or sulfamethoxazole. We note that all micropollutant test solutions were prepared from saturated aqueous stocks as described in the ESI.† Additional trials were conducted with atrazine in matrices more representative of environmental samples including model humic acid (up to 10 mg L^{-1} of Fluka humic acid) and alkalinity (5 mM carbonate).

Cross-flow filtration experiments with light irradiation were conducted for up to 3 h, during which 0.5 mL samples were taken periodically from the feed reservoir, retentate (*i.e.*, the cross-flow effluent that did not pass through the filter), and permeate (*i.e.*, the through-flow effluent that had passed through the filter) (see Fig. S1†). Solutions were pumped across and through the filter at equal rates, from 10 mL min^{-1} across and 10 mL min^{-1} through (540 L m^{-2} h^{-1} flux; within the range typical for microfiltration) up to 50 mL min^{-1} across and 50 mL min^{-1} through (2700 L m^{-2} h^{-1} flux). Flow rates were measured volumetrically (from the volume collected in a 10 mL graduated cylinder over 30 seconds) and controlled by adjusting the peristaltic pumping rate and a valve that regulated the amount of flow across and through the filter. Most experiments were operated with recirculation, where both filter permeate and retentate were returned to the magnetically stirred feed reservoir. A small subset of experiments with atrazine was also conducted without any recirculation, thereby allowing performance comparison of the filter when operating in a single pass or "dead end" filtration mode.

Prior to initiating all photocatalytic experiments, the solution was first circulated through the filter for 1 h in darkness to allow any sorption of the target analyte on the filter to reach equilibrium. UV and simulated sunlight control experiments were also conducted in which the system was operated and sampled without a C/TiO_2 filter to quantify transformation of organic contaminant targets by direct photolysis.

2.5. Analytical methods

Samples were analyzed *via* high performance liquid chromatography with a diode array detector (HPLC-DAD, Agilent 1100 Series) using methods adapted from previous work.[7,11] Additional HPLC method details are provided in the ESI.†

3. Results and discussion

3.1. Composite nanofiber characterization

3.1.1. Physical properties with varying mass loadings of TiO_2. Fig. 1 shows SEM images and histograms for C/TiO_2

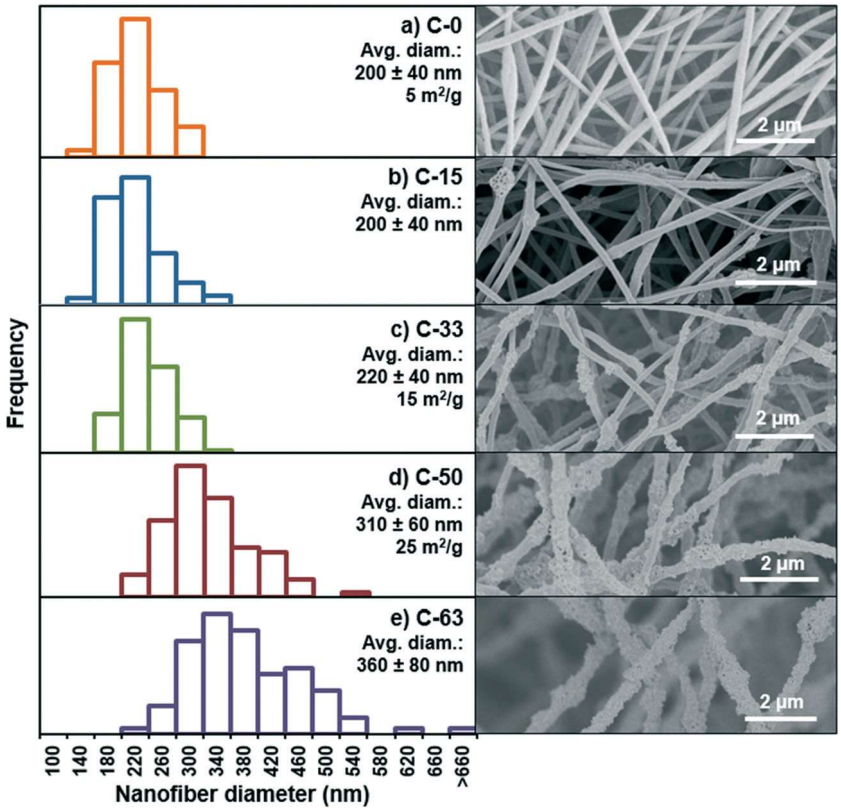

Fig. 1 Histograms and associated SEM images for (a) C-0 (0 wt% P25), (b) C-15, (c) C-33, (d) C-50, and (e) C-63 nanofiber composites. All electrospun sol gels contained 2.5 wt% PTA. As mass loading of P25 in the nanofibers increased, nanofibers transitioned from smooth carbon nanofibers, to rough nanofibers with visible TiO_2 aggregates and increased surface area.

composites with up to 63 wt% P25 (relative to PAN), denoted as C-(wt%) hereafter (*e.g.*, C-15 represents CNFs with 15 wt% P25). Each sol gel also contained 2.5 wt% PTA (the effects of which will be discussed in further detail below). Histograms of nanofiber diameter distributions reveal that below 33 wt%, the average diameter of C/TiO_2 nanofibers were roughly constant. In contrast, at higher P25 loadings average nanofiber diameter increased from ~200 nm to 360 ± 80 nm (at 63 wt% P25; see Fig. 1 and S3a†), suggesting there is a critical P25 mass above which the composite nanofiber morphology deviates from pure carbon nanofibers (or CNFs).

SEM images also revealed considerable differences in surface morphology of the nanofibers as P25 loading increased. Below C-33 (see Fig. 1a–c), the nanofibers appear to be predominantly carbon containing isolated aggregates of P25 nanoparticles (~400 nm in diameter), the number of which increased with P25 loading. Above C-33, more aggregates of P25 were observed on the surface of nanofibers, causing them to become visibly rougher. This transition from (primarily) isolated P25 aggregates in CNFs to more evenly distributed P25 aggregates likely contributes to the increase in diameter observed for these composites.

We note that the highest loading of P25 that could be electrospun was 80 wt% relative to PAN, and the resulting C-80 nanofibers are shown in Fig. S3b and c.† These nanofibers exhibited the most dramatic increase in diameter, with most measuring at ~1 μm. However, while composites with up to 63 wt% P25 remained moderately flexible based on routinely handling (*e.g.*, bending and flexing), higher P25 loadings (75 and 80 wt% P25) were especially brittle, chalky, and more susceptible to breaking while handling. Thus, they were not extensively utilized in subsequent flow-through reactivity studies because of concerns over their durability and likelihood to leach loosely bound P25 during application.

Analysis *via* XPS indicated just 0.3 atomic% (at%) Ti on the surface of C-15 nanofibers. Surface Ti concentration increased, albeit non-linearly, with increasing P25 content (Fig. 2a), with a more marked increase above 63 wt%. Specifically, surface Ti concentration more than doubled (from ~4 to ~9 at% Ti) over only a ~20 wt% increase in P25 content for C-63 and C-80 nanofibers. XPS suggests, therefore, that at low mass loadings the majority of P25 appears embedded within the bulk of the CNFs, and only at higher mass loadings (*i.e.*, above a 63 wt%) can more proportional increases in surface Ti be achieved *via* this synthesis approach.

Increases in P25 content also yielded composites with greater specific surface area, as measured by N_2 BET isotherms (measured surface areas are reported in Fig. 2b). While CNFs without P25 (*i.e.*, C-0) had rather low specific surface area (5 m^2 g^{-1}), the addition of P25 produced a linear increase in surface area for composites from 33 to 80 wt%. Thus, despite the corresponding increase in nanofiber diameter observed for these composites, the roughness imparted by the accumulation of P25 and P25 aggregates on the nanofiber surface yields considerable increases in composite surface area. Indeed, at the highest loadings investigated (C-80), as much as a 10-fold increase in surface area (to 50 m^2 g^{-1}) relative to C-0 was observed, a value roughly equivalent to the specific surface area we measured for P25 nanoparticles.

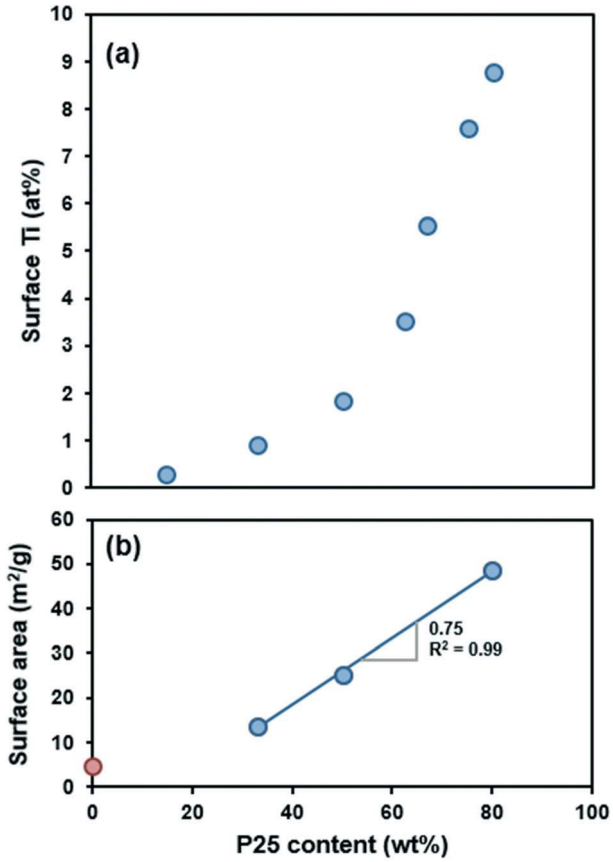

Fig. 2 (a) Surface concentration of Ti (atom% determined *via* XPS) and (b) surface area of C/TiO_2 nanofiber composites as a function of P25 content in the nanofibers. Above 63 wt% P25, increases in P25 corresponded with sharp increase in surface Ti. Surface area increased linearly between 33 wt% and 80 wt% P25 mass loadings in nanofibers.

Finally, XRD confirmed that the crystal structure of the embedded TiO_2 nanoparticles was not altered during nanofiber synthesis. Fig. S4† compares X-ray diffraction patterns for P25 nanoparticles and 5 nm TiO_2 nanoparticles to that of their composites. As expected from our prior work, X-ray diffraction patterns for P25 indicate a mixed phase consisting of both 75% anatase and 25% rutile.[7] In contrast, XRD results with 5 nm TiO_2 particles are indicative of pure anatase, while also showing the line broadening expected for smaller primary particle sizes (composites prepared from these 5 nm particles are discussed in the ESI,† with corresponding SEM images and histograms in Fig. S5†). In all C/TiO_2 composites, the XRD patterns were consistent with those obtained with respective TiO_2 starting materials, indicating that the carbonization step did not alter the phase of TiO_2 within the nanofibers.

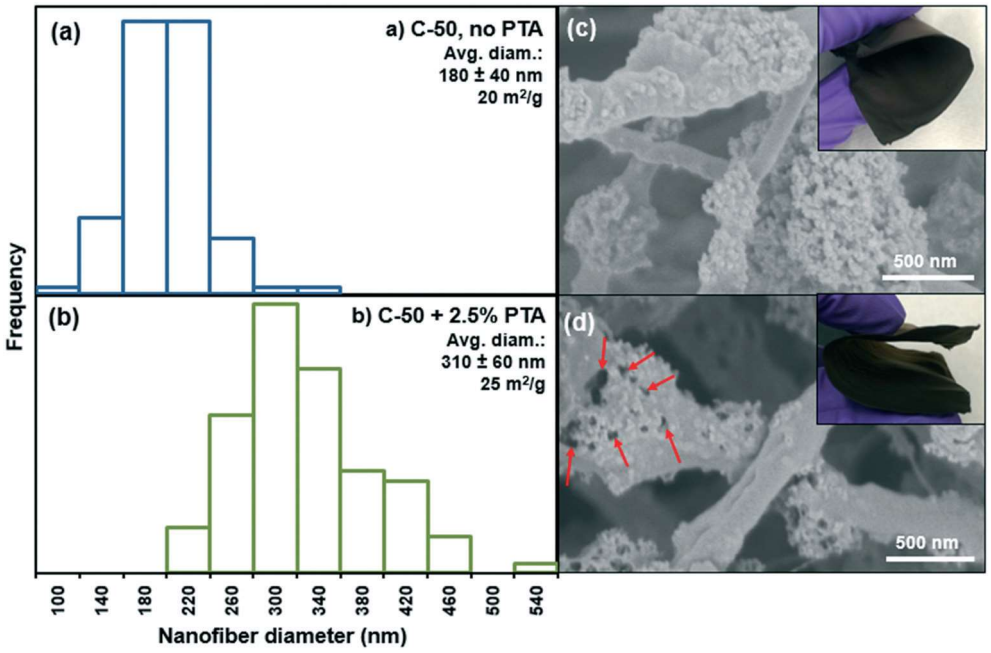

Fig. 3 Histograms, SEM images, and digital images of (a and c) C-50 without PTA and (b and d) C-50 with 2.5 wt% PTA. Pores introduced into nanofibers *via* PTA inclusion are indicated with red arrows in (d). Both materials remained flexible after stabilization/carbonization (see insets in c and d).

3.1.2. Structural benefits from inclusion of phthalic acid. The inclusion of 2.5 wt% PTA increased the average nanofiber diameter of C-50 from 180 ± 40 nm to 310 ± 60 nm (Fig. 3a and b), presumably due to the increase in precursor solution viscosity arising from its inclusion in the sol gel, as we have been previously observed.[11] Further, comparison of SEM images of C-50 with and without PTA suggest that PTA also introduces pores into the composite (Fig. 3c and d). This phenomenon is the result of PTA volatilization during carbonization and is known to increase not only surface area but also flexibility of CNFs and CNF composites.[11,34]

Unexpectedly, we also observed that PTA exerts a stabilizing effect on sol gel precursor suspensions containing P25. Higher mass loadings of P25, most notably C-80, could only be fabricated *via* electrospinning when PTA was present in precursor solutions at 2.5 wt%, whereas similarly high mass loadings without PTA produced an unstable (*i.e.*, aggregating and settling) precursor solution that could not be electrospun. Indeed, sedimentation studies conducted with P25 nanoparticles suspended in DMF illustrate that inclusion of PTA results in a more stable sol gel suspension (Fig. S6†). We conclude, therefore, that PTA, an aromatic dicarboxylic acid, sorbs to the P25 surface in suspension, thereby functioning as a stabilizing ligand in DMF. In water, PTA is known to form a bidentate surface complex on TiO_2,[35] and we presume a similar complex forms in polar DMF. Further, we propose that the ability of PTA to complex the P25 particle surface helps to promote the localization of macroporosity near the embedded P25 particles in the nanofiber composites; in fact, most pores observed in SEM images (see Fig. 3d) are located near regions of the nanofibers where P25 is clearly concentrated.

3.2. Optimization of C/TiO_2 reactivity

3.2.1. Optimization of UV photocatalytic composite material properties. In the recirculating configuration, the reservoir atrazine concentration generally followed exponential decay with UV irradiation time in all experimental filtration systems (Fig. 4a), behavior that was also observed for atrazine decay in closed (*i.e.*, no flow) batch systems with suspended P25 nanoparticles (Fig. S7a†). This was the case both in UV-only controls (*i.e.*, no C/TiO_2 composite filter) and in systems with C/TiO_2 filters across the range of P25 mass loadings investigated. We observed ~10% loss of atrazine through sorption to the C/TiO_2 filters (with the PVDF support) during the 1 h dark period prior to UV irradiation, and no additional atrazine loss *via* sorption occurred beyond 1 h suggesting sorption equilibrium was achieved. Moreover, UV light alone (*i.e.*, in the absence of C/TiO_2 composites) photolyzed ~30% of atrazine over 3 h (the standard time period utilized in reactive filtration experiments).

To compare reactivity across different C/TiO_2 filters, we calculated initial reaction rate coefficients (initial k_{obs} values) from the change in normalized atrazine concentration (*i.e.*, concentration at some time t divided by the initial concentration or C_t/C_0) in the reservoir over UV irradiation time, assuming pseudo-first-order decay. Because some filtration systems exhibited deviations from pseudo-first-order decay over longer filter run times, we typically limited our kinetic analysis to reservoir concentrations measured over the first hour of filter operation. These initial k_{obs} values were then corrected to account for measured atrazine loss from direct UV photolysis.

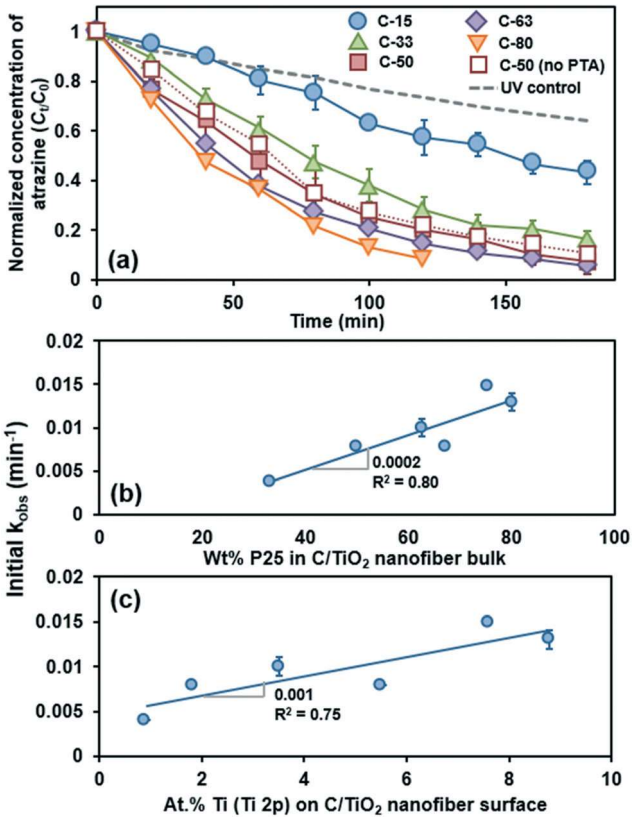

Fig. 4 (a) Curves showing phototransformation of 30 μg L^{-1} atrazine over time for C/TiO_2 nanofiber composites with different mass loadings of P25 (15 to 80 wt%), including C-50 without PTA. A UV control (conducted without C/TiO_2) is shown with the grey dashed line. (b) Observed initial rate constants (k_{obs}) as a function of P25 content of nanofibers, and (c) initial k_{obs} values as a function of surface Ti abundance determined *via* XPS. Rate coefficients correspondingly increased with increasing bulk and surface TiO_2.

Increasing the loading of P25 from 15 to 80 wt% correspondingly increased the reactivity of C/TiO_2 nanofibers toward atrazine upon exposure to UV light (Fig. 4a). Initial k_{obs} values increased from 0.004 to 0.013 min^{-1} over this range, corresponding to half-lives from ~50 min to 3 h. Assuming a steady-state concentration of hydroxyl radical ($[OH^{\bullet}]_{ss}$) on or near the surface of the UV-irradiated filter, these coefficients correspond to concentrations between 1×10^{-12} to 4×10^{-12} M. These values were estimated from our measured initial value of $k_{obs} = k_{OH}[OH^{\bullet}]_{ss}$, where k_{OH} is the reported second order rate constant for atrazine oxidation by hydroxyl radical of 3.17×10^9 M^{-1} s^{-1} from Cooper *et al.*[36] Notably, C/TiO_2 exhibited roughly equivalent initial k_{obs} values in experiments with initial atrazine concentrations ranging from 0.14 μM (30 μg L^{-1} or ppb) up to ~1.5 μM, supporting our use of a pseudo-first-order model to describe removal based on changes in reservoir concentration over time (Fig. S8†).

Generally, initial k_{obs} values increased with P25 content, expressed both as bulk P25 concentration (wt%) and surface Ti concentration (at%) from XPS (Fig. 4b and c). This is consistent with the larger abundance of P25 in the composite nanofibers being able to produce a greater concentration of hydroxyl radical (and possibly other reactive oxygen species known to be produced during P25 irradiation) at the nanofiber filter surface during UV irradiation. However, these correlations are not particularly strong, which may indicate that other physical and/or chemical factors influence atrazine degradation in these systems. For example, as P25 loading increases, so too does nanofiber diameter, which will influence the nominal pore size of the filter layer and potentially the degree of interaction between atrazine and the photocatalytic nanofiber surface.

Based on the moderate reactivity, ease of fabrication, and handling ability of C-50, this material was selected to evaluate the influence of other synthetic variables on composite performance. For example, as shown in Fig. 4a, the inclusion of PTA in C/TiO_2 had no impact on reactivity, while the use of 5 nm anatase TiO_2 in place of P25 rendered C/TiO_2 effectively unreactive as a photocatalyst (*i.e.*, degradation of atrazine was on par with the UV control experiment without any TiO_2 material present) (Fig. S7b†). Complementary experiments conducted in batch compared the reactivity of unsupported 5 nm anatase particles to P25, showing that under UV irradiation P25 is roughly 3-fold more reactive than the pure anatase particles (Fig. S7a†). This inherent difference in reactivity relates to mixed phase TiO_2 (anatase and rutile) being recognized as a superior photocatalyst than either pure rutile or pure anatase because of an electron trapping mechanism associated with the mixed phases.[37,38] Nevertheless, from these batch suspension results, we would anticipate some increase in atrazine removal for composites prepared from 5 nm anatase particles. We assume that the lack of reactivity in these composites may reflect the greater extent of aggregation (and thus, lower degree of surface availability) for 5 nm particles relative to P25, both in precursor sol gel solutions and upon integration into nanofiber composites.

As a final consideration, the performance of CNFs with embedded Au/TiO_2 particles was assessed. Despite clear increases in reactivity observed in closed batch systems for Au/TiO_2 relative to unmodified P25 particles (Fig. S9a†), no differences in reactivity were observed during photocatalytic filtration studies with Au/TiO_2 containing CNF composites (Fig. S9b†). We are left to assume that either the benefits of Au a co-catalyst are lost through the composite fabrication process (*e.g.*, during high temperature carbonization) or as a result of differences in the rate-determining step of atrazine degradation in suspended Au/TiO_2 batch systems and flow through systems with CNF supported Au/TiO_2 (*e.g.*, surface reaction *versus* surface sorption limited).

3.2.2. Optimization of photocatalytic filtration parameters. Various flow rates in the recirculating cross-flow filtration system were assessed to determine optimal conditions for removal of atrazine as a model organic pollutant (Fig. 5). During each run, atrazine concentrations were measured over time in the reservoir, retentate, and permeate. This sampling regime allowed us to assess C-50 (electrospun with 2.5 wt%

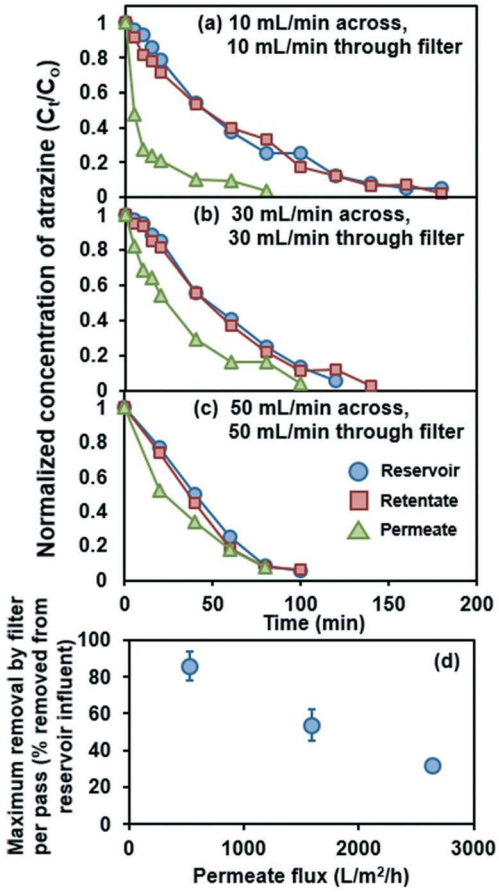

Fig. 5 Normalized concentration of atrazine (with initial 30 μg L^{-1} concentration) over time in cross-flow filtration reservoir, retentate, and permeate for (a) 10 mL min^{-1}, (b) 30 mL min^{-1}, and (c) 50 mL min^{-1} retentate and permeate flow rates. Although more removal is achieved overall with high flow rates (c), low flow rates correspond with more removal in a single pass through the filter [as measured from the difference in reservoir and permeate concentrations at each time point (a)]. (d) Maximum removal of atrazine in a single pass through the filter as a function of permeate flux. Only 540 L m^{-2} h^{-1}, the leftmost point with the highest maximum removal, falls within the range of microfiltration.

PTA) filter performance in a recirculating cross-flow configuration by monitoring changes in reservoir concentration over time. It also allowed us to evaluate the extent of atrazine removal in a single pass through the irradiated filter by comparing the difference between the reservoir and permeate concentrations at each sampling point.

Although the relatively high flow rates of 50 mL min^{-1} across and through the filter achieved the fastest overall decrease in atrazine concentration in the reservoir (non-detect after 1.5 h), this configuration benefited from high filter throughput to overcome relatively limited (~20%) removal of atrazine with each pass through the UV-irradiated filter. In comparison, at flow rates of 10 mL min^{-1} across and through the filter, the reservoir concentration of atrazine reduced more gradually (non-detect after 3 h) because of less volume being passed through the filter over time. However, filter permeate immediately exhibited much lower concentrations of atrazine, achieving as much as 80% atrazine removal in a single pass. Indeed, the maximum atrazine removal achieved in a single pass decreased considerably at higher flow rates (*i.e.*, higher values of permeate flux) (see Fig. 5d), presumably because the contact time between the atrazine solution and the irradiated C-50 filter layer is greatest at lower flux (estimated residence times in the ~600 μm thick filter layer were between approximately 1.2 and 6 s for the highest and lowest flow rates, respectively). So that we could continue to assess micropollutant removal in a single filter pass, we conducted all additional experiments at this lower flow rate of 10 mL min^{-1} across and through the filter.

To minimize the amount of filter mass required for treatment, we also explored the performance of C-50 nanofiber filters with half (~300 μm) and three-times (1800 μm) the thickness of our standard recipe for composite filter fabrication (*i.e.*, that used during previously discussed optimization experiments; ~600 μm). At a flow rate of 10 mL min^{-1}, filters with cross-sectional widths of 290 ± 20, 600 ± 40, and 1800 ± 200 μm as determined by SEM (corresponding to filter residence times ranging from ~3 to 18 s) all exhibited comparable reactivity toward atrazine (Fig. S10†), with an initial k_{obs} value estimated from reservoir atrazine concentrations of ~0.011 min^{-1}. This suggests that the photoactive zone (*i.e.*, the depth of the composite filter layer exposed to light) is likely less than ~300 μm, perhaps even considerably, such that any increases in filter thickness beyond this depth provide little additional performance benefit. While we tried to explore the performance of even thinner filter layers, composites thinner than ~300 μm could not be electrospun using our approach because the material was too thin to be removed from the collector without damaging it. Due to its efficacy and the minimal amount of material needed to prepare 300 μm thick filters (which corresponds to only ~30 mg of composite), this filter thickness was used in all subsequent flow-through studies.

Additional tests evaluated material performance during irradiation with wavelengths available in sunlight (using a 305 nm long-pass, cut-on filter). Fig. S11† compares the time-dependent removal of atrazine in a single filter pass (determined from the difference in reservoir and permeate concentration at each sampling point) for C-50 filters under UV and simulated sunlight. As expected UV light resulted in greater atrazine removal, but filters exposed to wavelengths of light greater than 305 nm were still able to remove between 20–50% of atrazine in a single pass. Notably, under both UV and >305 nm irradiation, the extent of atrazine removal in a single pass through the C-50 filter layer increased over time (see Fig. S11†). The timescales of our experiments should be sufficient to achieve steady-state $^{\bullet}OH$ production at or near the filter surface during irradiation, such that the available $^{\bullet}OH$ concentration should be reasonably constant over time. Instead, the increase in

atrazine removal per filter pass over time likely reflects this near-constant level of $^{\bullet}OH$ reacting with a decreasing concentration of atrazine in the filter influent over time. Consistent with such a scenario, we observed near-constant removal of atrazine in a single pass through the filter (~40% loss compared to ~10% in dark controls) in a limited number of UV light experiments where the filtration system was operated without recirculation (*i.e.*, permeate was not returned to the feed reservoir; see Fig. S12†).

3.3. Performance of optimized nanofiber filters in environmentally relevant matrices and toward a suite of organic micropollutants

Filtration trials with atrazine in the presence of natural organic matter (10 mg L^{-1} Aldrich humic acid) and alkalinity (250 mg L^{-1} as $CaCO_3$ at pH 9.5; typical conditions for tap water in our laboratory at the University of Iowa) revealed no influence on atrazine removal by C-50 filters (300 μm thickness) over time in UV-irradiated systems (see Fig. S12†). Performance of these C-50 nanofiber filters was also assessed using recirculating, cross-flow UV-filtration (flow rates of 10 mL min^{-1} across and through the filter) for the photochemical oxidation of solutions containing either 0.5 μM atrazine, benzotriazole, caffeine, carbamazepine, DEET, metoprolol, naproxen or sulfamethoxazole. Normalized concentration profiles of each pollutant in the reservoir, retentate, and permeate, along with UV controls (without C-50 present), are shown in Fig. 6. After equilibration for 1 h to allow for sorption, ~10% of atrazine and ~15% of DEET sorbed to filters, while all other compounds did not measurably sorb. Sulfamethoxazole was susceptible to direct photolysis, degrading by 80% over 3 h with exposure to UV light alone. Direct UV photolysis occurred to a lesser extent

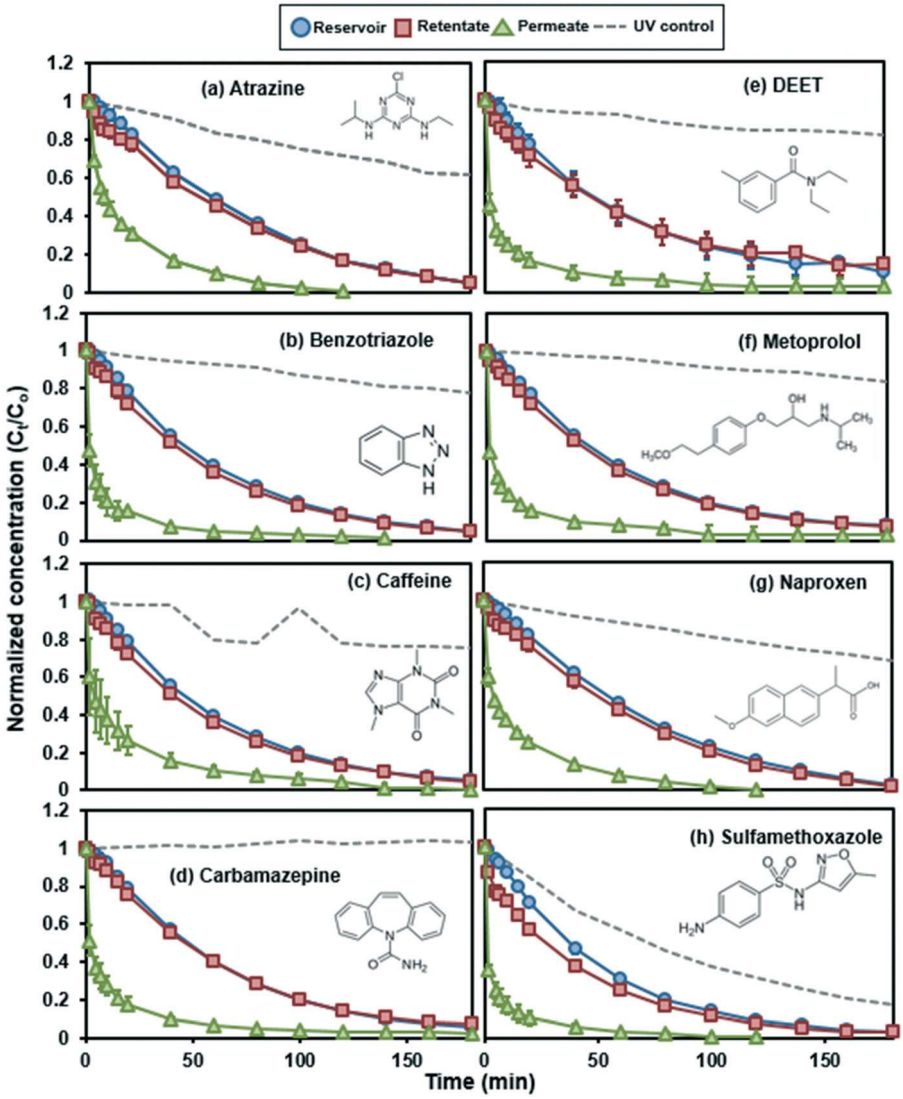

Fig. 6 Normalized concentration of chemical contaminants over time in cross-flow filtration reservoir, retentate, and permeate with initial 0.5 μM (a) atrazine, (b) benzotriazole, (c) caffeine, (d) carbamazepine, (e) DEET, (f) metoprolol, (g) naproxen, and (h) sulfamethoxazole. UV controls, conducted without C/TiO_2 present, are shown by grey dashed lines.

for atrazine (~30%), benzotriazole (20%), caffeine (25%), DEET (20%), metoprolol (15%), and naproxen (30%) over a 3 h period, while carbamazepine was stable.

In the presence of C-50, the permeate had considerably reduced concentrations of each micropollutant as compared to the reservoir and retentate early in the trials (Fig. 6). The notable decrease in sulfamethoxazole in retentate as compared to the reservoir was due to the impact of direct UV photolysis on concentration within the quartz filtration cell. Overall, the micropollutant suite exhibited half-lives [$t_{1/2}$ values = $\ln(2)/k_{obs}$] ranging from 45 min to 1 h in the recirculating flow through system, based on trends in reservoir concentration over time.

Using the difference at each sampling point between retentate and permeate concentration, Fig. S13† illustrates the time-dependent removal of each micropollutant in a single pass through the UV-irradiated C-50 filter. As observed earlier with atrazine (see Fig. S11†), the extent of removal in a single pass generally increases over time as micropollutant concentrations in the feed reservoir become depleted over time, in turn increasing the relative abundance of $^{\bullet}OH$ available at the filter surface to drive pollutant transformation. However, the extent of micropollutant removal in a single pass appears to stabilize between 60 to 90% across the analyte suite after ~30 minutes of filter operation. We assume that pollutant removal in this regime becomes limited by the transport of the micropollutant to the near surface region of the irradiated C-50 filter where $^{\bullet}OH$ concentrations are greatest. Indeed, initial k_{obs} values for micropollutant removal (from reservoir concentrations) do not appear to scale with reported second-order rate constants for the oxidation of each micropollutant with hydroxyl radical (*i.e.*, k_{OH} values)[39] (Fig. S14†). This likely implies that reaction with $^{\bullet}OH$ is not rate-limiting in the UV-irradiated filter system, and that other steps in the reaction sequence (*e.g.*, micropollutant surface adsorption or product desorption) primarily control the overall rate of pollutant transformation in our system.

4. Conclusions and environmental implications

Herein, we optimize and evaluate the performance of photochemically reactive TiO_2/carbon nanofibers, a stand-alone platform for use in applications where simultaneous filtration and chemical oxidation is desired. Electrospinning enabled a simple, single-pot synthesis of these photoactive composites, while stabilization and carbonization converted PAN, a polymer support susceptible to oxidative stress, into a more resistant carbon nanofiber ideal for advanced oxidation processes. The reactivity of C/TiO_2 nanofiber filters was tunable and could be enhanced by increasing photocatalytic TiO_2 loading within nanofibers (ultimately aided by inclusion of PTA as a stabilizing agent and porogen in electrospinning precursor solutions). An advantage of these filters is the relatively low mass of material required to achieve this level of treatment; optimal reactivity herein was obtained with only 30 mg of composite mass in a filter 0.3 mm thick.

Addressing current and emerging challenges in water treatment, composite filters reveal relatively strong (60–90% removal in a single pass) performance toward a broad spectrum of organic micropollutants (atrazine, benzotriazole, caffeine, carbamazepine, DEET, metoprolol, and naproxen) generally known for their recalcitrance to more traditional forms of water treatment. We have also demonstrated the versatility of these materials across varying water quality (*e.g.*, NOM and alkalinity) and process flows, with high pollutant removal in a single pass akin to dead-end filtration at low flow rates or *via* a recirculating, cross-flow system at higher flows. Although not extensively investigated, for atrazine we also observed evidence (Fig. S15†) that transformation products can be subsequently degraded during recirculation, suggesting the potential to minimize formation of unwanted byproducts. We note that the extent of pollutant transformation achieved herein was accomplished at concentrations (500 nM) that are still high relative to typical values observed for micropollutants in sources used for drinking water (typically 10's of ng L^{-1} to 100's of μg L^{-1}). Our data suggest that a key factor in the extent of pollutant removal achieved in a single pass is the relative amount of photooxidants (*e.g.*, $^{\bullet}OH$) compared to the influent micropollutant concentration, where the rate of reaction with $^{\bullet}OH$ in the near-surface region is fast and does not appear to be rate-limiting. Thus, in systems with lower micropollutant concentrations, we would anticipate comparable, and perhaps even greater, degrees of removal in a single pass through the irradiated C/TiO_2 filter, although such assumptions need to be validated in systems with lower (*e.g.*, ng L^{-1}) micropollutant concentrations and with micropollutant mixtures.

We anticipate that these findings will translate to systems beyond the bench scale testing apparatus used herein. Electrospinning is a mature fabrication route viable at industrial scales,[40] which should enable filter production for a range of applications in water treatment [from point-of-use and point-of-entry (POU/POE) to larger treatment systems]. In considering POU/POE applications, which are ideal for the small technology footprint of these nanofiber composites, results herein can be used to preliminarily assess the scale and performance of a treatment system used in home. Considering an influent with atrazine at a level 10-fold greater than the US EPA MCL (0.14 μM or 30 μg L^{-1}), k_{obs} values measured herein can be used to estimate the amount of time needed to achieve safe drinking water with atrazine levels below the MCL. Using our standard 30 mg C-50 filter to treat 500 mL of water (or 0.06 g of C/TiO_2 per liter of water treated), we estimate a clean water production rate of 0.13 L h^{-1}. Furthermore, if the average consumer drinks 2 L of water a day, it would only take ~44 grams (or ~0.01 lbs) of C/TiO_2 per year to treat an individual's water supply to a safe level of atrazine at this production rate. Of course, a larger filtration system using more mass of C/TiO_2 per liter of water would

increase the clean water production rate of such a POU/POE system. We find these estimates encouraging, although certainly more work is needed to produce C/TiO_2 nanofibers at the scale necessary to validate the performance of such a photoactive treatment system. Assuming a suitable photoreactive filtration design can be developed, the performance of C/TiO_2 and its stability over longer application run times more typical of an individual's water treatment needs (*i.e.*, over days to years) will also need to be validated at deployment scale.

Conflicts of interest

There are no conflicts to declare.

Acknowledgements

This work was supported by the U.S. EPA (grant number R835177) and by NSF 1804757 and 2040464. K. E. G. was supported by a University of Iowa (UI) Presidential Graduate Research Fellowship and through funding from the Donald E. Bently Professorship at UI.

References

1 A. Eslami, M. M. Amini, A. Asadi, A. A. Safari and N. Daglioglu, Photocatalytic degradation of ibuprofen and naproxen in water over NS-TiO_2 coating on polycarbonate: Process modeling and intermediates identification, *Inorg. Chem. Commun.*, 2020, **115**, 107888.

2 A. T. Nguyen and R.-S. Juang, Treatment of o-Cresol/4-chlorophenol binary mixtures in aqueous solutions by TiO_2 photocatalysis under UV irradiation, *Desalin. Water Treat.*, 2016, **57**(15), 6820–6828.

3 Z. Zhao, Y. Wang, J. Xu and Y. Wang, Mesoporous Ag/TiO_2 nanocomposites with greatly enhanced photocatalytic performance towards degradation of methyl orange under visible light, *RSC Adv.*, 2015, **5**(73), 59297–59305.

4 S. K. Loeb, P. J. J. Alvarez, J. A. Brame, E. L. Cates, W. Choi, J. Crittenden, D. D. Dionysiou, Q. Li, G. Li-Puma, X. Quan, D. L. Sedlak, T. David Waite, P. Westerhoff and J.-H. Kim, The Technology Horizon for Photocatalytic Water Treatment: Sunrise or Sunset?, *Environ. Sci. Technol.*, 2019, **53**(6), 2937–2947.

5 M. R. Wiesner, G. V. Lowry, P. Alvarez, D. Dionysiou and P. Biswas, Assessing the risks of manufactured nanomaterials, *Environ. Sci. Technol.*, 2006, **40**(14), 4336–4345.

6 Y. Zhang, Y. Chen, P. Westerhoff, K. Hristovski and J. C. Crittenden, Stability of commercial metal oxide nanoparticles in water, *Water Res.*, 2008, **42**(8), 2204–2212.

7 M. J. Nalbandian, K. E. Greenstein, D. Shuai, M. Zhang, Y.-H. Choa, G. F. Parkin, N. V. Myung and D. M. Cwiertny, Tailored Synthesis of Photoactive TiO2 Nanofibers and Au/TiO_2 Nanofiber Composites: Structure and Reactivity Optimization for Water Treatment Applications, *Environ. Sci. Technol.*, 2015, **49**(3), 1654–1663.

8 K. E. Greenstein, N. V. Myung, G. F. Parkin and D. M. Cwiertny, Performance comparison of hematite (α-Fe_2O_3)-polymer composite and core-shell nanofibers as point-of-use filtration platforms for metal sequestration, *Water Res.*, 2019, **148**, 492–503.

9 C. Sun, N. Wang, S. Zhou, X. Hu, S. Zhou and P. Chen, Preparation of self-supporting hierarchical nanostructured anatase/rutile composite TiO_2 film, *Chem. Commun.*, 2008, 3293–3295.

10 J. Qian, B. Jennings, D. M. Cwiertny and A. Martinez, Emerging investigator series: development and application of polymeric electrospun nanofiber mats as equilibrium-passive sampler media for organic compounds, *Environ. Sci.: Processes Impacts*, 2017, **19**(11), 1445–1456.

11 K. T. Peter, J. D. Vargo, T. P. Rupasinghe, A. De Jesus, A. V. Tivanski, E. A. Sander, N. V. Myung and D. M. Cwiertny, Synthesis, Optimization, and Performance Demonstration of Electrospun Carbon Nanofiber–Carbon Nanotube Composite Sorbents for Point-of-Use Water Treatment, *ACS Appl. Mater. Interfaces*, 2016, **8**(18), 11431–11440.

12 C.-G. Lee, H. Javed, D. Zhang, J.-H. Kim, P. Westerhoff, Q. Li and P. J. J. Alvarez, Porous Electrospun Fibers Embedding TiO_2 for Adsorption and Photocatalytic Degradation of Water Pollutants, *Environ. Sci. Technol.*, 2018, **52**(7), 4285–4293.

13 A. E. Deniz, A. Celebioglu, F. Kayaci and T. Uyar, Electrospun polymeric nanofibrous composites containing TiO_2 short nanofibers, *Mater. Chem. Phys.*, 2011, **129**(3), 701–704.

14 J. S. Im, M. I. Kim and Y.-S. Lee, Preparation of PAN-based electrospun nanofiber webs containing TiO_2 for photocatalytic degradation, *Mater. Lett.*, 2008, **62**(21), 3652–3655.

15 M. Lombardi, P. Palmero, M. Sangermano and A. Varesano, Electrospun polyamide-6 membranes containing titanium dioxide as photocatalyst, *Polym. Int.*, 2011, **60**(2), 234–239.

16 Y. Hong, D. Li, J. Zheng and G. Zou, Sol–gel growth of titania from electrospun polyacrylonitrile nanofibres, *Nanotechnology*, 2006, **17**(8), 1986–1993.

17 F. Mehrpouya, H. Tavanai, M. Morshed and M. Ghiaci, The formation of titanium dioxide crystallite nanoparticles during activation of PAN nanofibers containing titanium isopropoxide, *J. Nanopart. Res.*, 2012, **14**(8), 1074.

18 X. Meng, N. Luo, S. Cao, S. Zhang, M. Yang and X. Hu, In-situ growth of titania nanoparticles in electrospun polymer nanofibers at low temperature, *Mater. Lett.*, 2009, **63**(16), 1401–1403.

19 C. Su, Y. Tong, M. Zhang, Y. Zhang and C. Shao, TiO_2 nanoparticles immobilized on polyacrylonitrile nanofibers mats: a flexible and recyclable photocatalyst for phenol degradation, *RSC Adv.*, 2013, **3**(20), 7503–7512.

20 A. Abdal-hay, H. M. Mousa, A. Khan, P. Vanegas and J. H. Lim, TiO_2 nanorods coated onto nylon 6 nanofibers using hydrothermal treatment with improved mechanical properties, *Colloids Surf., A*, 2014, **457**, 275–281.

21 L. Szatmáry, J. Šubrt, V. Kalousek, J. Mosinger and K. Lang, Low-temperature deposition of anatase on nanofiber materials for photocatalytic NOx removal, *Catal. Today*, 2014, **230**, 74–78.

22 H. Zhang and L. Yang, Immobilization of nanoparticle titanium dioxide membrane on polyamide fabric by low

temperature hydrothermal method, *Thin Solid Films*, 2012, **520**(18), 5922–5927.

23 S. Kim and S. K. Lim, Preparation of TiO_2-embedded carbon nanofibers and their photocatalytic activity in the oxidation of gaseous acetaldehyde, *Appl. Catal., A*, 2008, **84**(1), 16–20.

24 C. Su, X. Ran, J. Hu and C. Shao, Photocatalytic Process of Simultaneous Desulfurization and Denitrification of Flue Gas by TiO_2–Polyacrylonitrile Nanofibers, *Environ. Sci. Technol.*, 2013, **47**(20), 11562–11568.

25 M. H. Tai, P. Gao, B. Y. L. Tan, D. D. Sun and J. O. Leckie, A Hierarchically-Nano Structured TiO2-Carbon Nanofibrous Membrane for Concurrent Gravity-Driven Oil-Water Separation, *Int. J. Environ. Sci. Dev.*, 2015, **6**(8), 590–595.

26 S. Ramasundaram, A. Son, M. G. Seid, S. Shim, S. H. Lee, Y. C. Chung, C. Lee, J. Lee and S. W. Hong, Photocatalytic applications of paper-like poly(vinylidene fluoride)-titanium dioxide hybrids fabricated using a combination of electrospinning and electrospraying, *J. Hazard. Mater.*, 2015, **285**, 267–276.

27 L. T. Memetea, N. C. Billingham and E. T. H. Then, Hydroperoxides in polyacrylonitrile and their role in carbon-fibre formation, *Polym. Degrad. Stab.*, 1995, **47**(2), 189–201.

28 Y. Gu, C. Li, J. Bai, J. Wang and T. Ma, One-step solvothermal synthesis of Au-TiO_2 loaded electrospun carbon fibers to enhance photocatalytic activity, *Vacuum*, 2016, **130**, 1–6.

29 C. H. Kim, B.-H. Kim and K. S. Yang, TiO_2 nanoparticles loaded on graphene/carbon composite nanofibers by electrospinning for increased photocatalysis, *Carbon*, 2012, **50**(7), 2472–2481.

30 J. Melcher, S. Feroz and D. Bahnemann, Comparing photocatalytic activities of commercially available iron-doped and iron-undoped aeroxide TiO_2 P25 powders, *J. Mater. Sci.*, 2017, **52**(11), 6341–6348.

31 M. J. Benotti, R. A. Trenholm, B. J. Vanderford, J. C. Holady, B. D. Stanford and S. A. Snyder, Pharmaceuticals and Endocrine Disrupting Compounds in U.S. Drinking Water, *Environ. Sci. Technol.*, 2009, **43**(3), 597–603.

32 R. L. Oulton, T. Kohn and D. M. Cwiertny, Pharmaceuticals and personal care products in effluent matrices: A survey of transformation and removal during wastewater treatment and implications for wastewater management, *J. Environ. Monit.*, 2010, **12**(11), 1956–1978.

33 P. Westerhoff, Y. Yoon, S. Snyder and E. Wert, Fate of Endocrine-Disruptor, Pharmaceutical, and Personal Care Product Chemicals during Simulated Drinking Water Treatment Processes, *Environ. Sci. Technol.*, 2005, **39**(17), 6649–6663.

34 H. Liu, C.-Y. Cao, F.-F. Wei, P.-P. Huang, Y.-B. Sun, L. Jiang and W.-G. Song, Flexible macroporous carbon nanofiber film with high oil adsorption capacity, *J. Mater. Chem. A*, 2014, **2**(10), 3557–3562.

35 K. D. Dobson and A. J. McQuillan, In situ infrared spectroscopic analysis of the adsorption of aromatic carboxylic acids to TiO_2, ZrO_2, Al_2O_3, and Ta_2O_5 from aqueous solutions, *Spectrochim. Acta, Part A*, 2000, **56**(3), 557–565.

36 W. J. Cooper, S. A. Snyder, S. P. Mezyk, J. R. Peller and M. G. Nickelsen, Reaction Rates and Mechanisms of Advanced Oxidation Processes (AOPs) for Water Reuse, Project Report 04–17, Water Reuse Foundation, 2010, Available at: https://watereuse.org/watereuse-research/04–17-reaction-rates-and-mechanisms-of-advanced-oxidation-processes-aops-for-water-reuse/.

37 D. C. Hurum, A. G. Agrios, K. A. Gray, T. Rajh and M. C. Thurnauer, Explaining the Enhanced Photocatalytic Activity of Degussa P25 Mixed-Phase TiO_2 Using EPR, *J. Phys. Chem. B*, 2003, **107**(19), 4545–4549.

38 D. O. Scanlon, C. W. Dunnill, J. Buckeridge, S. A. Shevlin, A. J. Logsdail, S. M. Woodley, C. R. A. Catlow, M. J. Powell, R. G. Palgrave, I. P. Parkin, G. W. Watson, T. W. Keal, P. Sherwood, A. Walsh and A. A. Sokol, Band Alignment of Rutile and Anatase TiO_2, *Nat. Mater.*, 2013, **12**(9), 798–801.

39 S. Mandal, Reaction Rate Constants of Hydroxyl Radicals with Micropollutants and Their Significance in Advanced Oxidation Processes, *J. Adv. Oxid. Technol.*, 2018, **21**(1), 178–195.

40 L. Persano, A. Camposeo, C. Tekmen and D. Pisignano, Industrial Upscaling of Electrospinning and Applications of Polymer Nanofibers: A Review, *Macromol. Mater. Eng.*, 2013, **298**(5), 504–520.